nature communications

Article

https://doi.org/10.1038/s41467-024-55199-6

Sub-millimeter fiberscopic robot with integrated maneuvering, imaging, and biomedical operation abilities

Received: 22 June 2024

Accepted: 3 December 2024

Published online: 30 December 2024

Check for updates

Tieshan Zhang[1,2,3,6], Gen Li[1,2,3,6], Hao Ren[2], Liu Yang[1,3], Xiong Yang[1,3], Rong Tan[1,3], Yifeng Tang[2], Dong Guo[2], Haoxiang Zhao[1,3], Wanfeng Shang[4,5] & Yajing Shen[1,3]

Small-scale continuum robots hold promise for interventional diagnosis and treatment, yet existing models struggle to achieve small size, precise steering, and visualized functional treatment simultaneously, termed an "impossible trinity". This study introduces an optical fiber-based continuum robot integrated imaging, high-precision motion, and multifunctional operation abilities at submillimeter-scale. With a slim profile of 0.95 mm achieved by microscale 3D printing and magnetic spray, this continuum robot delivers competitive imaging performance and extends obstacle detection distance up to ~9.4 mm, a tenfold improvement from the theoretical limits. Besides, the robot showcases remarkable motion precision (less than 30 μm) and substantially widens the imaging region by ~25 times the inherent view. Through ex vivo trials, we validate the robot's practicality in navigating constrained channels, such as the lung end bronchus, and executing multifunctional operations including sampling, drug delivery, and laser ablation. The proposed submillimeter continuum robot marks a significant advancement in developing biomedical robots, unlocking numerous potential applications in biomedical engineering.

Small-scale continuum robots provide an alternative choice for interventional diagnosis and treatment in the body[1–3] owing to their narrow cavity-accessing ability, bringing superiorities of quick recovery, and low infection risk. Up to date, the treatment of several diseases has been demonstrated using small continuum robots, such as heart disease treatment through deploying stent or electrophysiology catheter[4], repair of perforation of gastric and duodenal ulcers by single-port laparoscopy[5], maxillary sinus disease treatment by natural orifice transluminal endoscopic surgery (NOTES)[6], and cerebrovascular disease diagnosis through whole-brain angiography[7], etc. However, despite the small continuum robots bring promising prospects of small contour, precise steering, and visualized treatment, it remains a great challenge for a robot can have all these three significant specifications at the same time, resulting in an impossible trinity.

Lots of actuation methods, such as tendon[8,9], fluid[10,11], smart materials[12], and magnetic field[13–15], are able to control the continuum robots for active steering. By integrating the camera and surgical tools at the end of robot's body[5], these robots are capable of performing several functional tasks, such as diagnostic and treatment potentials. Nevertheless, it's difficult to maintain the contour as small as a submillimeter scale due to the limitation of camera size and fabrication technology, resulting in them not being able to access the narrow pathological areas with a diameter smaller than 2.0 mm in the body,

[1]Department of Electronic and Computer Engineering, Hong Kong University of Science and Technology, Hong Kong SAR, China. [2]The Robot and Automation Center and the Department of Biomedical Engineering, City University of Hong Kong, Hong Kong SAR, China. [3]Center on Smart Manufacturing, Hong Kong University of Science and Technology, Hong Kong SAR, China. [4]National Engineering Laboratory of Big Data System Computing Technology, Shenzhen University, Shenzhen, China. [5]Shenzhen Institute of Advanced Technology (SIAT), Chinese Academy of Science (CAS), Shenzhen, China. [6]These authors contributed equally: Tieshan Zhang, Gen Li. e-mail: eeyajing@ust.hk

such as lung end bronchus[16] and oviduct[17]. The magnetic polymer-based guidewire[13] and hydraulically actuated microcatheter[18] are capable of being established with a submillimeter contour. Yet, such a small size is realized by scarifying the functions, that they lack the ability for in situ diagnosis and treatment for lesions due to the absence of integrated vision and surgical tools. The optical fiber-based probe can be made very small and can either provide imaging[19–21] (e.g., microstructure investigation inside the arteries[22]) or surgical functions (e.g., laser delivery/ablation[23,24]). Nevertheless, it remains a challenge to integrate these two functions within a fiber probe limited by the fabrication technology, haltering the real-time treatment. Moreover, the fiber itself doesn't have the ability of active steering. Although introducing the continuum robots can improve maneuverability, their size will be increased to several millimeters[25], resulting in difficulty in accessing narrow pathological areas.

Herein, to unravel the "impossible trinity" (Fig. 1a), we present an optical fiber-based continuum robot with submillimeter-scale contour that can perform high precision motion and carry out multifunctional operations in situ, capable of accessing constrained channel environments in the body, e.g., lung end bronchial area (Fig. 1b). This work initially lays out the integrated design and miniaturized fabrication for the probe robot. By employing the technologies of microscale 3D printing and magnetic spray, we achieved the probe contour with a 0.95 mm diameter while granting it with magnetic response (Fig. 1c). Next, the characteristics of imaging and out-of-sight navigation of the probe have been verified. Later, we showcase the high-precision motion of the robot under magnetic actuation and demonstrate the local scanning and stitching performance. Finally, with an ex vivo porcine model experiment, we have demonstrated the proposed continuum robot's capability of accessing constrained channel, e.g., lung end bronchus, and carrying out in situ operations. This study inspires the design of small-scale continuum robot for accessing more hard-to-reach areas in the body and enriches broad potential biomedical applications.

Results

Design and fabrication of the submillimeter robotic probe by 3D printing and magnetic spray

As illustrated in Fig. 1d, the proposed submillimeter probe mainly consists of an optical fiber array for imaging, a hollow skeleton for deploying fibers, and a functionalized skin for controlling. To achieve a miniaturized design, we fabricate a submillimeter hollow skeleton (Outer diameter ~0.75 mm) for deploying the optical fiber array by micro-scale 3D printing (Fig. S1a). To control the motion of the probe precisely, we proposed the strategy of functionalized skin. Firstly, a layer of magnetic elastomer (Thickness ~0.075 mm) is covered on the surface by employing magnetic spray[26], granting the probe active steering capacity under a magnetic field while keeping almost no increase in its contour (Fig. S1c). Then, a layer of hydrogel skin (Thickness ~0.025 mm) is further coated on the outer surface of the robot body to create the hydrophilic characteristic to reduce the potential friction during the intervention process (Fig. S1e). Lastly, to fulfill the functions, we optimize the hollow skeleton to deploy different types of optical fibers and micro-tubes for imaging and visualized treatment (Fig. S6a). With a central fiber bundle and several circular deployed light guide fibers, the capacity of in situ imaging (Fig. 1d–i) can be utilized for disease diagnosis. Besides, by embedding a laser fiber or micro-tube, the laser or fluidic drug can then be delivered to the pathological target, carrying out the visualized treatment (Fig. 1d (ii, iii, iv)). Consequently, we can obtain the functionalized submillimeter probe robot with a 950 μm diameter that can achieve active navigation and in situ treatment at the same time, unraveling the "impossible trinity".

To achieve a uniform image in front, the fiber bundle (labeled in light blue) should be arranged in the central and the light guide fibers (labeled in light green) be distributed around it (Fig. 2a)[27]. Yet, due to the small divergence/acceptance angle of the fiber, the effective imaging zone A_{effect} (labeled in light red) is usually much smaller than the theoretical imaging area A_{img} (labeled in light blue). Adding lenses on the tip of the fibers is a possible solution to enlarge the imaging zone[28], but it requires manufacturing and assembling multiple groups of complex lenses on the tip of each fiber for light collimation and/or beam focusing/expansion, which is quite difficult at the submillimeter scale. Here, we proposed an alternative strategy by optimizing the layout of the probe to obtain a large imaging area with a simple system setup and high stability in real practice. Furthermore, we also proposed a local scanning and stitching method with the assistance of the magnetic field to capture the image of the target that is folds of times larger than the probe view.

As illustrated in Fig. 2b–e, increasing the number of lighting fibers n_{f} will accordingly increase the effective projection area A_{effect} at a certain distance (4.5 mm in this example, Fig. 2b). Yet, we find that such an increase becomes less and less with the increase of n_{f} because the effective imaging zone becomes closer to a virtual circle with a radius of R_{vir} (theoretical analysis is given in Supplementary Note S2). Particularly, the maximum ratio $ra_{\mathrm{proj}} = A_{\mathrm{effect}}/A_{\mathrm{img}}$ remarkably increases from 36.8% (single fiber) to 72.4% (three fibers), and the improvement becomes smaller after that. For instance, the relative increment of the ratio is over 35% when the fiber changes from two to three while the value is below 17% afterward. (Fig. 2e). It implies that the benefit of embedding more light guide fibers is limited when the number is larger than three. On the other hand, the mechanical strength of the skeleton would decrease significantly with the increase of the channels for lighting fiber (Fig. 2f–h) due to the sub-millimeter size of the probe (the thickness of the shell is only 35 μm). Considering we need to reserve one more channel on the probe for functional tools, the number of fiber channels should be smaller than a certain number to guarantee mechanical strength and working reliability. Our analysis reveals that the skeleton with four peripheral holes ($n_{\mathrm{f}} = 3$) has neglectable strength decline compared to the one embedding two light guide fibers, e.g., the affordable loads decrease at normal/lateral/torsional forms are only 4.2%, 0.2%, and 1.1%, respectively (Fig. 2i–k). Therefore, by comprehensively considering the imaging, strength, and function, we finally deployed four peripheral holes, composed of three uniformly circumferential arranged holes (No. 1, 2, and 3) for light guide fibers and another hole (with 180° of hole 1 and at the same radial distance) for functional tools (Fig. 1d) to achieve imaging and treatment simultaneously.

Interventional imaging and out-of-sight navigation inside narrow channel

The optical system for imaging mainly consists of the medical cold light source, fiber coupler, camera, objective lens, and the probe, as shown in Figs. 3a and S9. Particularly, the optical fiber coupler is designed in one input and three output manner (1 × 3) to uniformly introduce the light source into the embedded three light guide fibers. The objective lens 20x is designed to enlarge and collimate the light information transmitted from the fiber bundle for better coupling the camera. To achieve pose adjustment of the 20x lens in the imaging path, a four-degree-of-freedom (4DOF) (X-Y-Z-θ) adjustable base is assembled as the support. Besides, the functional channel is left for customized integration for certain treatments. Such design can obtain a better coupling effect of the light path of the optical system and therefore, achieve in situ imaging and treatment of the pathological area simultaneously.

To investigate the light transmission profile of the probe, we established its virtual direct radiation model and analyzed the effect of the distance ds and the offset dr on the light intensity distribution (Fig. 3b, Supplementary Note S5). The results indicate that the flux first increases and then decreases as the distance ds increases, and the peak

https://doi.org/10.1038/s41467-024-55199-6

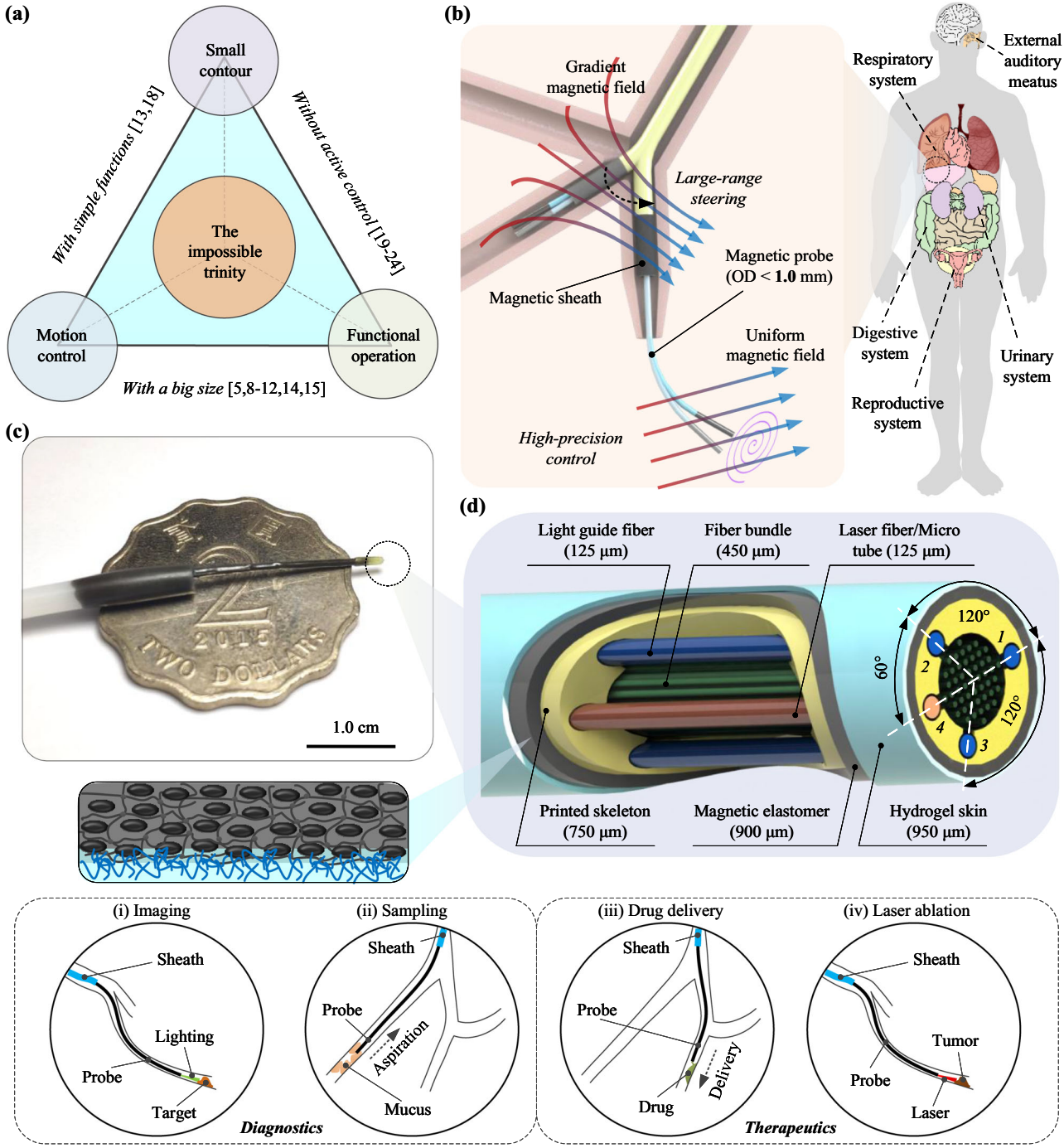

Fig. 1 | Overview of the optical fiber-based sub-millimeter continuum robot with imaging, maneuvering, and medical operation capabilities. a Achieving small contour, high-precision motion control, and visualized functional operations simultaneously poses a challenge for robots, referred to as the "impossible trinity". **b** Schematics of the proposed sub-millimeter continuum robot driven by multi-sectional magnetic fields for medical diagnosis and treatment in narrow channels. **c** Image depicting the probe tip, over a two-dollar Hong Kong coin. **d** Schematic of the probe tip, comprising of a central fiber bundle, three light guide fibers (No. 1, 2, 3), and an additional functional tool channel (No. 4) within the skeleton fabricated by microscale 3D printing technology. A thin layer of magnetic elastomer is coated on the probe for actuation, and then a thin hydrogel layer is covered on the outer surface to reduce the friction. The manufactured probe boasts a diameter contour of 0.95 mm. The diagnostic and therapeutic potential of the fiberscopic robot include (**i**) imaging, (**ii**) sampling, (**iii**) drug delivery, and (**iv**) laser ablation.

value appears at ~1 mm from the tip of the probe. It also implies that the flux increases with the increase of the offset till $d_r = 0.225$ mm (the radius of the fiber bundle) while remaining stable after that. For instance, as the curves shown in Fig. 3c, the corresponding peak flux increases from 0.13×10^{-10} lm to 6.9×10^{-10} lm with d_r changing from −0.2 mm to 0.225 mm. We also evaluated the light intensity at different d_s and d_r by designing a testing system with a movable platform for holding the reflective board and an X-Y-Z-θ adjustable base for fixing the probe (Fig. S12a). The experiment results (Fig. 3d) show a good coincidence with the theoretical analysis, suggesting that the peak intensity, denoting the complete overexposure status of the camera, presents at ~1 mm from the probe tip. Thus, the maximum imaging region shall be within this distance to get a clear image. Within the imaging zone, the object, e.g., a number symbol of "5" with a size

https://doi.org/10.1038/s41467-024-55199-6

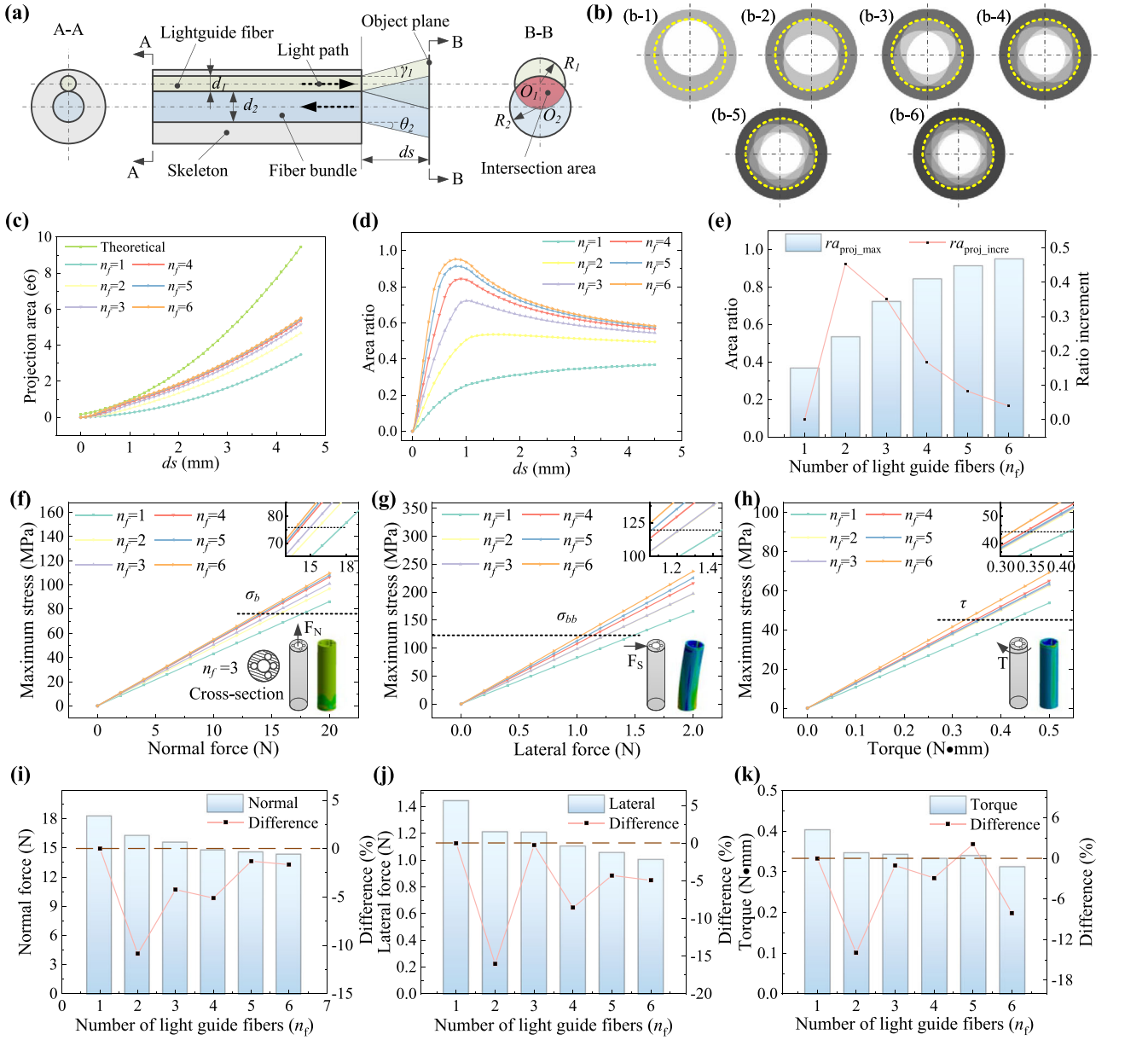

Fig. 2 | Design and characteristics of the probe. a Schematic of light path transmission through the probe embedded with a central fiber bundle (labeled in light blue) and a light guide fiber (labeled in light green). A-A sectional view shows the geometrical layout and B-B sectional view shows the light covering status on the object plane, where the intersection area (labeled in light red) denotes the effective imaging region. **b** The theoretical projection area on the object plane at 4.5 mm when using different numbers of light guide fibers. The outer gray and the inner white area denote the theoretical imaging region and the effective imaging region, respectively. **c** The projection area variation against distance using different numbers of fibers. **d** The ratio of the effective imaging zone over the theoretical imaging zone against distance. **e** The analytical comparison of the maximum area ratio with different numbers of light guide fibers, which suggests that the effective image area increase is not significant after the number of fibers is more than three. The finite element analysis (FEA) results of the skeletons with different hollow structures under normal force (**f**), lateral force (**g**), and torque load (**h**). The insets in the corner are the FEA simulation results of the skeleton with four peripheral holes. The analytical comparison of the mechanical strength of the skeletons with different hollow structures when reaching the normal (**i**), lateral (**j**), and torsional (**k**) stress limit. After considering the balance between imaging, strength, and function, we finally developed the skeleton structure with a central lumen for fiber bundle, three uniformly circumferential arranged holes for light guide fibers and another hole for functional tools. Source data are provided as a Source Data file.

~250 μm, can be clearly captured by the proposed imaging system, as shown in Fig. 3a.

To achieve effective and safe steering, the exploration ability in a farther region than the theoretical maximum imaging distance (1 mm) is also essentially significant for identifying the branches and obstacles to make proper decisions (e.g., entrance or bypass) in advance. To address this challenge, we proposed an intensity distribution-based environment exploration strategy and extended the blur obstacle detection distance ~10 folds farther to ~9.4 mm (see Supplementary Note S6.1 for detail). As illustrated in Fig. 3e, when an object is offset placed in front, the collected light through the central fiber bundle is different, i.e., the intensity will be higher if the object is positioned in this quadrant, or will be lower if a free channel is in front. Thus, we can take the collected intensity as the parameter to forecast the environment though there is no clear image. To demonstrate it, we divide the endoscopic view into four quadrants, i.e., top left (TL), top right (TR), bottom left (BL), and bottom right (BR) (Fig. 3e). By analyzing the variation of both the separate intensity and the corresponding

https://doi.org/10.1038/s41467-024-55199-6

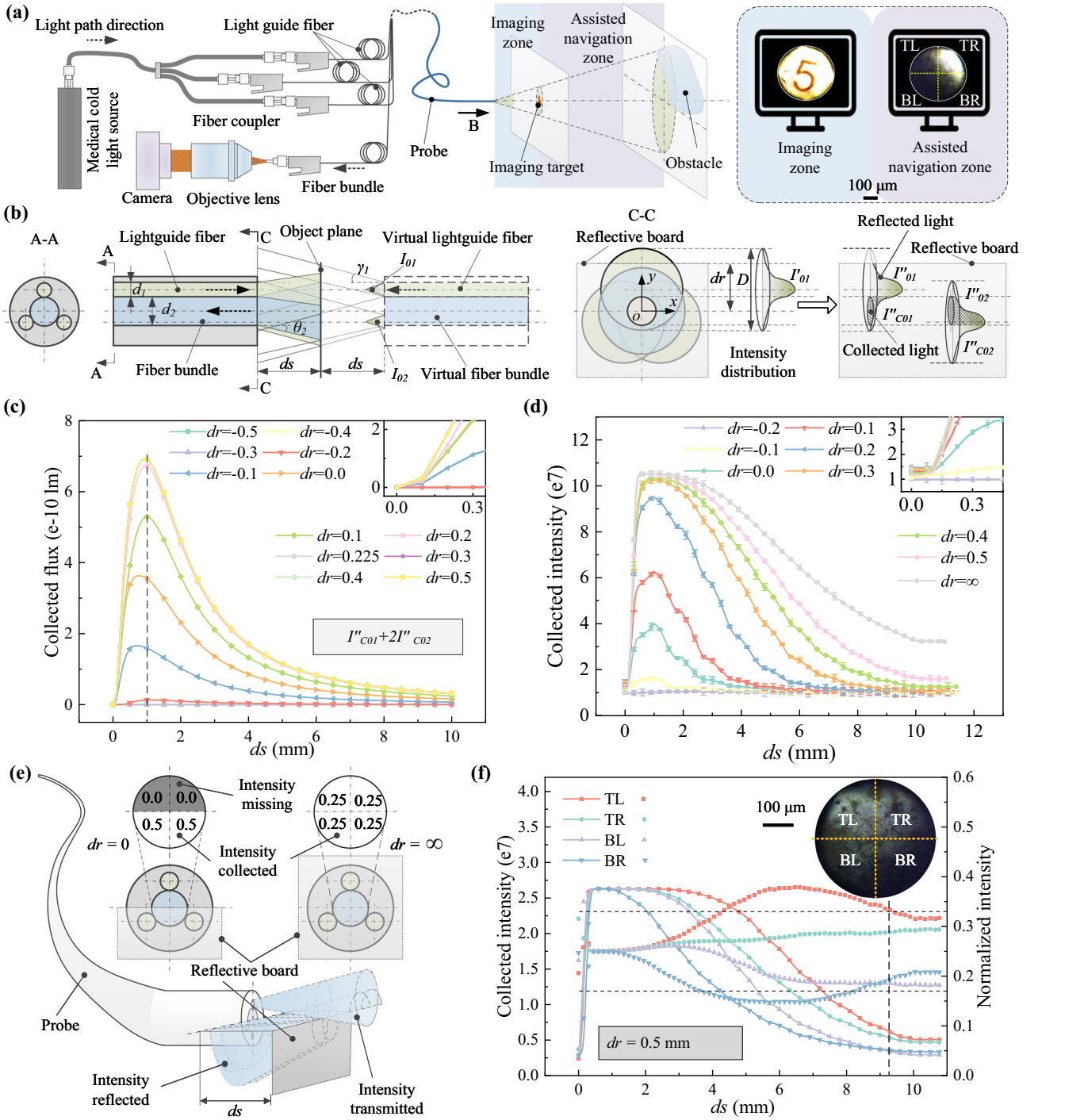

Fig. 3 | Imaging system characterization of the probe. a Schematic representation of the endoscopic imaging system and the depiction of the corresponding imaging zone and assisted navigation zone in front of the probe. Results illustrate the capture of number symbol "5" within the imaging zone, and the detect of an obstacle positioned beyond the imaging zone. **b** Illustration of the transmission principle of light intensity distribution through the proposed probe, with a reflective board positioned at a distance *ds* and an offset *dr* from the probe tip and its central plane, respectively. **c** Theoretical representation of the light intensity collected by the central fiber bundle against distance *ds* and lateral offset *dr* of the reflective board. The dashed line denotes the theoretical limit of imaging clearly. **d** Experimental measurement of the collected light intensity against distance *ds* and lateral offset *dr* of the reflective board, exhibiting a similar trend with the theoretical one. Data are represented as mean values ± s.d. from three samples. **e** Principle of the proposed intensity distribution-based environment exploration strategy for identifying objects beyond the imaging zone, e.g., an evenly normalized intensity of 0.25 would be obtained for the four quadrants if a reflective obstacle fully covers the probe tip. **f** Analytical evidence confirming the existence and orientation of the object beyond the imaging zone with an offset of 0.5 mm. The normalized intensity from the TL quadrant is ~0.33 at a distance of ~9.4 mm, indicating an obstacle in the top left direction in front of the probe, despite being out-of-sight. TL, TR, BL, and BR represent top left, top right, bottom left, and bottom right, respectively. The dashed line on the corner denotes the farthest distance of ~9.4 mm, where an object in front can still be estimated the relative orientation. Source data are provided as a Source Data file.

normalized value from the four quadrants, we can not only identify whether there is an obstacle in front but also estimate its relative orientation to the probe. For instance, an object with a 0.5 mm lateral offset while at a distance of about 9.4 mm can still have its rough orientation estimated as being in the top left quadrant, based on the fact that the normalized intensity in this quadrant exceedes the threshold (Fig. 3f, Fig. S13, Supplementary Note S6.1).

High precise positioning, image scanning, and stitching based on multi-sectional magnetic steering

The motion of the continuum robot is regulated by two sets of magnetic actuation systems, i.e., the magnetic sheath and magnetic probe. The former one is actuated by a permanent magnet to achieve a large movement range and the latter one is actuated by a three-degree-of-freedom (3DOF) Helmholtz coil to achieve high accuracy (Figs. 4a and S26). As depicted in Fig. 4a, when the M-spray coated sheath is positioned within the gradient magnetic field created by an external magnet, it will generate an induced magnetization $\mathbf{m}_{\mathrm{sh}}$ along its axial direction. Thus, the sheath will be subjected to both the magnetic force F_{msh} and magnetic torque T_{msh}, guiding its tip towards the magnetic source with bending (Supplementary Note S8). As a result, by controlling the gradient magnetic field applied on the magnetic sheath, we can control the position and orientation of the sheath tip effectively. On the other hand, the magnetic probe experiences only magnetic torque T_{mde} when placed in the workspace of the coil system. With the induced magnetization $\mathbf{m}_{de}$ along its axial direction, the torque tends to bend the probe tip to align its axis with the uniform magnetic field within the workspace. By adjusting the dynamic current applied to each coil, thereby controlling the magnitude and direction of the uniform magnetic field, we can precisely steer the probe tip to follow predefined trajectories, e.g., a circular path (labeled as the red dot curve) (Supplementary Note S8).

To assess the motion precision of the continuum robot under magnetic actuation, we first tested the motion of magnetic sheath. The results show that a root mean square error (RMSE) of ~0.25 mm and ~2.2° for the tip's position and orientation can be achieved respectively (Fig. S25), verifying the continuum robot' potential to perform navigation within confined channel environments. To further evaluate the precision of the probe tip's movement, we set up a vertical perspective recording system consisting of two orthogonally placed microscopes inside the Helmholtz coil system, as illustrated in Figs. 4b and S26. The experimental results indicate that the probe is able to follow linear trajectories with a RMSE of less than 20 μm (Fig. S27). To exhibit its motion precision in 3D space, we designed three typical trajectories for testing, i.e., squares, circles, and spirals, as depicted in Fig. 4c–e. The results confirmed that, even in the worst-case scenario, we can maintain a comprehensive RMSE of ~30 μm.

The high-precision motion capabilities allow the robot to transcend the visual limitations inherent in the conventional fiber bundle contour. As depicted in Fig. 4f, leveraging the high positioning accuracy of the magnetic probe (<30 μm), the position of the probe's view in each frame can be accurately predicted. By designing a scanning trajectory, specifically an Archimedes spiral trajectory[29] in this instance to achieve a higher scanning efficiency, the full information of the sample in a larger view can be obtained after seamless stitching of images. To demonstrate it, we present an example of a Bauhinia flower pattern with a diameter of ~3.0 mm (Fig. 4f). By imaging one of its leaves, we clearly showcase the full image of the leaf (Fig. 4g, Supplementary Movie 1) with a RMSE of less than 9 pixels (Fig. S31). This significant expansion of the imaging region represents ~25 folds increase compared to the original fiber bundle's viewing capacity, paving a practical and effective solution to overcome the constraints of limited imaging areas.

To demonstrate the magnetic navigation and imaging capacity of the proposed robotic system, we fabricated a 1:1 transparent bronchial tree model to carry out the interventional experiment (Figs. 4h and S33). As the results shown in Fig. 4i, with the cooperation of the rear-end advancing platform and the applied gradient magnetic field, the continuum robot can successfully pass the bifurcations (P1 and P2) and reach the imaging target (P3) at $t = 262$ s, carrying out the task of in situ imaging later (a grid pattern with a side length of 200 μm can be seen in Fig. 4i-2). Then, after retrieving to the first bifurcation P1, the robot is steered to the right bronchus channel and finally reach the end bronchus to find the thrombus (P5, denoted by a red clot) at $t = 685$ s (Supplementary Movie 2).

Functional demonstration of sampling, drug delivery, and laser ablation in an ex vivo porcine model

Leveraging the small size, active steering, and imaging abilities, the proposed robot shows promise in facilitating early and effective diagnosis and treatment of hard-to-reach diseases within narrow passages, e.g., lung end bronchial diseases[30]. Specifically, benefiting from the specialized design of the probe tip, we are able to incorporate a functional channel with a diameter of ~130 μm into the wall of the probe, with minimal compromise to its mechanical integrity. This strategy enables seamless integration of tailored surgical instruments, catering to a variety of therapeutic requirements. To demonstrate it, we conducted a series of in vitro/ex vivo experiments correspondingly using a printed bronchial tree model and a porcine lung model, including tasks such as sampling, drug delivery, and laser ablation, utilizing different medical tools deployed through the functional channel (Fig. 5a). These in vitro experimental results can be seen in Supplementary Note S11.3, Fig. S38 and Supplementary Movies 3 and 4. Besides, throughout those ex vivo trials, we employed digital subtraction angiography (DSA, CGO-2100, Beijing Wandong Medical Equipment Co., Ltd) to monitor the probe's position and movements.

Liquid biopsy[31], a specialized form of bio-sampling, stands as a crucial method for disease diagnosis. However, certain diseases, such as non-small-cell lung cancer, which develops within narrow channels with small diameters, pose challenges for conventional instruments due to their big size. To tackle this obstacle, we incorporated a micro tube (ID/OD: 50/100 μm; referred to as "tool-I") into the functional channel of our probe and established a dedicated pumping subsystem for aspiration (Fig. S34). By inserting the microtube into a capillary tubing sleeve (ID/OD: 110/1600 μm) and securely fastening it with a microfluidic connector, we created a sealed fluidic channel. Subsequently, a rubber tube (ID/OD: 1.0/1.5 mm) was utilized to convey fluids from the connector to a syringe attached to an injection pump. By controlling the injection pump to retract the syringe plunger, negative pressure was generated inside, facilitating aspiration through the integrated microtube. The intervention results are illustrated in Fig. S39, where the DSA images confirm the successful access of the probe tip into the end bronchus, which has an inner diameter of ~1.0 mm. Furthermore, the probe detects the presence of small air bubbles within the bronchus (Figs. 5b–2). By maintaining a negative pressure ~55 KPa within the syringe established by the injection pump (extract 3 mL air in the chamber) for ~2 min, ~7.0 μL of fluids were collected. Upon images under an optic microscope, we observe viscous characteristics and the encapsulation of numerous micrometer-scale air bubbles (Figs. 5b–3, Supplementary Movie 5, part I). In a clinical context, the accumulation of mucus within the airways could serve as a means to identify early pathological symptoms of certain lung disease[32].

Targeted drug delivery is an efficient and precise therapy strategy[33,34], but treating the diseases in the narrow channel is still challenging due to the accessing difficulty. Leveraging the sub-millimeter contour, our proposed robot offers a promising solution to address this hurdle. Through the integration of a microtube (ID/OD: 50/100 μm; referred to as "tool-II") within the probe and the

https://doi.org/10.1038/s41467-024-55199-6

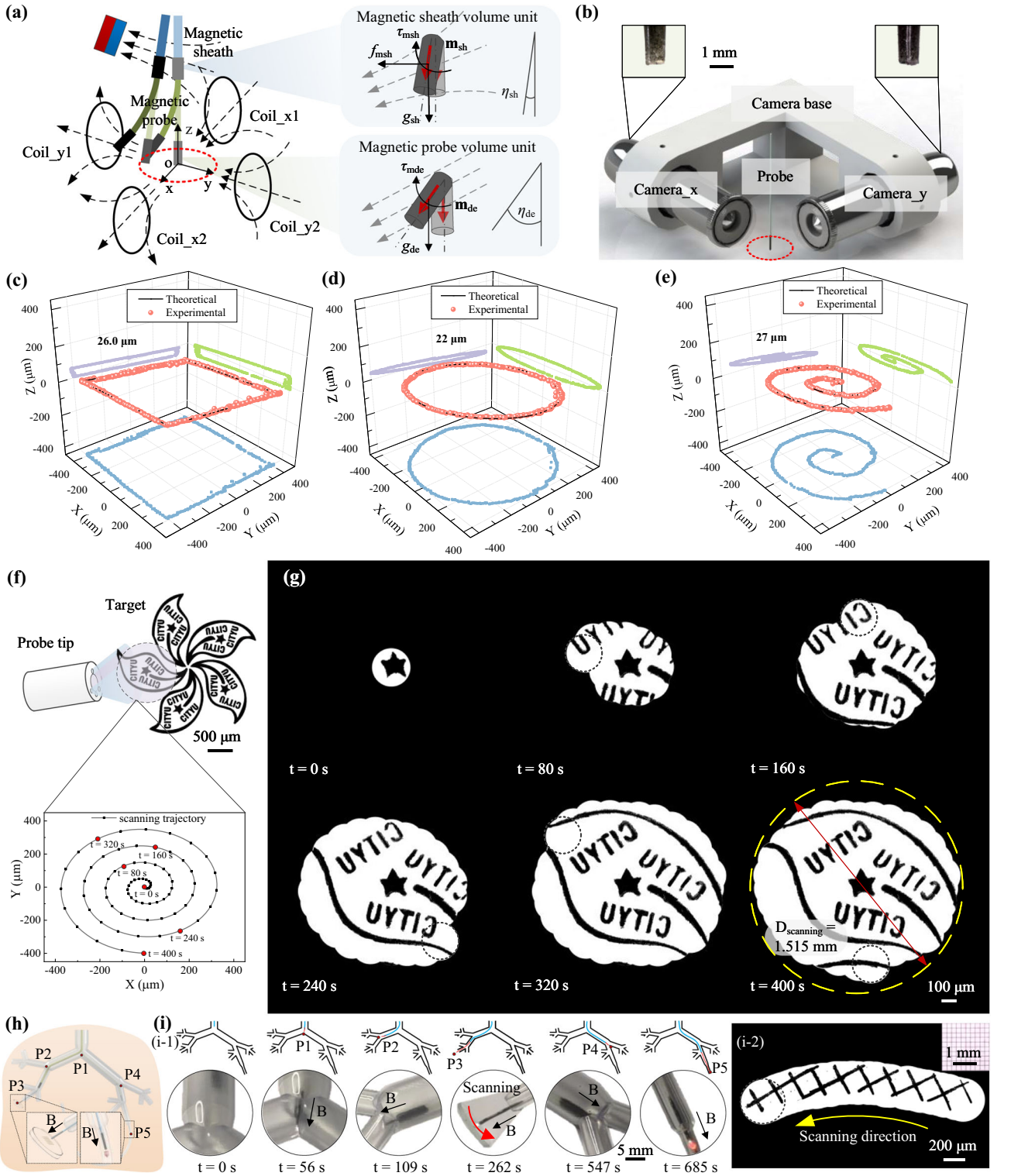

Fig. 4 | High precise maneuvering of the continuum robot. a Schematic depicting the multi-sectional actuation by the magnetic field. The magnetic sheath is actuated by a gradient magnetic field to achieve large-range steering, while the magnetic probe is actuated by a uniform magnetic field to achieve high-precision motion. **b** Experimental setup for evaluating the probe's motion trajectory. Path tracking results of the probe tip under square (**c**), circle (**d**), and spiral (**e**) trajectories, presenting a motion error of less than 30 μm for complex 3D trajectories. The light blue, green, and purple dots here correspond to the projection in the x-o-y plane, x-o-z plane, and y-o-z plane of the recorded trajectories. **f** Schematic illustrating sample scanning by a designed Archimedes spiral trajectory. **g** Reconstruction results (one leaf of a Bauhinia flower) utilizing the local scanning and stitching strategy, achieving a ~25-fold expansion of view. **h** Schematic of the interventional procedure performed by the continuum robot in an in vitro bronchial tree model. **i** Experimental snapshot of the interventional process and the scanning result of a grid pattern. Source data are provided as a Source Data file.

https://doi.org/10.1038/s41467-024-55199-6

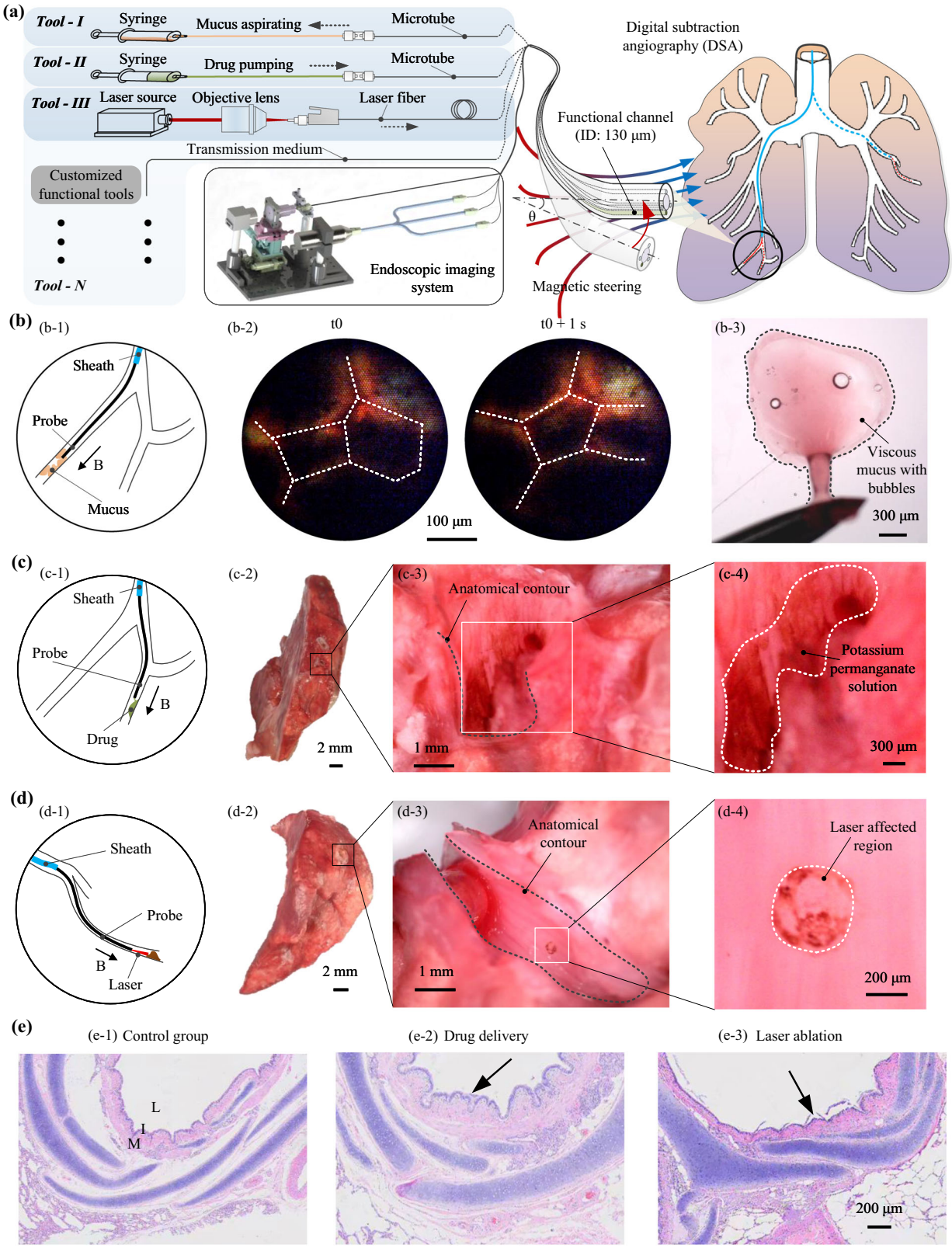

improvement of the aforementioned pumping subsystem, introducing a pressure sensor to the fluidic channel for monitoring and avoiding excessive pressure, liquid drugs can be efficiently pumped from the syringe to the probe tip. To demonstrate the drug delivery process (Fig. 5c), we begin by filling 1.0 mL of the liquid drug, i.e., potassium permanganate solutions in this case, into the syringe. After introducing an additional 3.0 mL air chamber, we regulated the injection pump to establish a ~100 KPa positive pressure inside the syringe for ~10 min. Subsequently, ~20 μL of the solutions were delivered. Anatomical observations reveal that the drug, distinguished by its brown color, is clearly visible on the inner surface of the end bronchus (Figs. 5c–4, Supplementary Movie 5, part II). With this successful demonstration, we envision the utilization of various drugs to achieve therapeutic objectives in practical settings in the future.

Fig. 5 | Functional demonstration of the continuum robot in an ex vivo porcine model. a Schematic illustrating the multifunctional integration of the proposed continuum robot and its demonstration in ex vivo intervention under magnetic actuation. Various functions can be achieved by integrating different types of medical tools. **b** Schematic representation of the mucus sampling (b-1) inside the end bronchus (ID: ~1.0 mm). The detected air bubbles by the probe suggest the existence of mucus (b-2). The aspirated sample exhibits viscous characteristic and embedded microscale bubbles (b-3), verifying endoscopic recording. Similar results can be found in repeated three times experiments. **c** Schematic depicting drug delivery (c-1) inside an end bronchus. Anatomical results of the end bronchus (c-2) demonstrate successful delivery of the drug (potassium permanganate solutions, brown color after oxidization) on its inner surface (c-3, 4). **d** Schematic of laser ablation (d-1) within an end bronchus. Anatomical examination of the bronchus (d-2) reveals ablation results (a scar of ~300 μm diameter) caused by the laser on the inner surface (d-3, 4). **e** H&E results further confirm the effectiveness of drug delivery and laser ablation, i.e., the deeper grooves (e-2) and the debris (e-3) show significant difference compared to normal bronchus tissue (e-1). Similar results can be found in repeated three times experiments. L, I, M denote bronchus lumen, ciliated endothelium, and muscle matrix, respectively.

Laser ablation is also a promising therapeutic approach, offering treatment for lesions with low complication risk and swift postoperative recovery[35]. However, delivering a laser source to the pathological target situated within a confined environment presents a significant challenge due to the lack of efficient tools. To alleviate the issue, we integrate a laser fiber (OD: 125 μm; referred to "tool-III") into the probe's functional channel and establish the corresponding laser subsystem (Fig. S36). To demonstrate the laser ablation process, a near-infrared laser source (808 nm, 6×8 mm^2) is initially secured on the optical base. Subsequently, a 10× objective lens is installed along the light path to focus it as a point laser source. The proximal end of the laser fiber is then fixed within a two-DOF (X-Y) adjustable lens support and at a distance of 2 mm from the lens, facilitating precise coupling of the focused laser. Upon reaching the end bronchus (inner diameter of ~1.0 mm), the laser source is activated for ~15 min (Fig. 5d). Subsequent anatomical examination reveals a small scar with a diameter of ~300 μm on the inner surface of the bronchus (Figs. 5d–4, Supplementary Movie 5, part III), thus confirming the efficacy of laser ablation in the narrow channel.

To further validate our findings, we conducted pathological section experiments on the treated bronchus tissue. The H&E staining results revealed notable distinctions between the normal bronchus structure and the areas subjected to drug delivery and laser ablation (Fig. 5e). In the control group, the bronchial structure exhibited typical features including the bronchus lumen, ciliated endothelium, and muscle matrix, denoted as "L", "I", and "M" respectively. However, following drug delivery, the endothelium displayed increased wrinkling with deeper grooves, indicating the oxidizing effect of the potassium permanganate solutions. Conversely, laser irradiation resulted in a smoother endothelium with visible debris, indicative of tissue damage caused by the high-energy laser.

With its integrated customized functionalities, such as sampling, drug delivery, and laser ablation, among others, the proposed submillimeter probe showcases substantial potential for conducting in situ diagnosis and therapeutic interventions on pathological tissue, such as within the lung end bronchus regions. Its versatility and precision render it a promising tool for early detection and treatment, with the potential to revolutionize the management of various diseases within challenging-to-access channel environments.

Discussion

Small-scale continuum robots are regarded as promising tools for interventional diagnosis and treatment, but existing robots struggle to achieve small size, precise steering, and visualized functional treatment simultaneously, termed an "impossible trinity". In this study, we introduced a continuum robot that successfully overcomes the apparent conflict between a small contour, high-precision control, and functional operations. To achieve the desired small contour, we adopted the fiber array as the core element and utilized the microscale 3D printing technology to fabricate the probe tip skeleton. To control the probe with high precision and a large motion range, we proposed a two-sectional magnetic actuation system. Lastly, to meet the requirements of in situ functional operations, we integrated a functional channel within the probe for various surgical tools. Leveraging the above three features of our robot, we can finally achieve successful navigation inside the lung bronchial tree model and carry out in situ surgical operations within the end bronchus with a size of ~1.0 mm.

Due to the inherent contour limitation of the fiber bundle, the field of vision of existing fiber-based imaging systems usually cannot provide sufficient information on the pathological area. Leveraging the probe's high-precision motion, we proposed a strategy of local scanning and stitching, enlarging the overall imaging region by ~25 folds. This strategy not only enhances the diagnostic potential of the robot through scanning imaging of pathological areas but also opens up possibilities for precise in situ surgical manipulations. Despite these advantages, the reported stitching approach here would potentially slow down the scanning speed and be prone to body's movements. In this manuscript, we have demonstrated the feasibility of this approach for enlarging the imaging area. In future work, we will address this challenge by: optimizing the image processing algorithm to enhance stitching efficiency; designing the scanning path as a denser spiral trajectory with smaller gaps between adjacent curves to minimize information loss; and upgrading the stitching algorithm by integrating both trajectory and image features to improve accuracy.

In this manuscript, we demonstrate its narrow channel accessing and imaging capability and showcase its potential to perform multiple surgical operations within the end bronchus, encompassing sampling, drug delivery, and laser ablation. Notably, the integration of additional tools, apart from the microtube and laser fiber, within the functional channel of the proposed continuum robot enables it to facilitate a wide range of functions. This work is expected to provide a significant solution for the development of a clinical surgical robot aimed at achieving early diagnosis and therapeutic goals in more hard-to-reach bodily regions, thereby enriching the broad potential for biomedical applications.

Methods

Fabrication of the soft continuum robot

To fabricate the proposed magnetic continuum robot, we first utilized micro-scale 3D printing technology to create the hollow skeleton of the probe tip (Fig. S1a). Using the nanoArch S140 printing system (BMF Material Technology Inc., Shenzhen, China) along with the photosensitive resin HTL (material parameters detailed in Supplementary Table S3), we achieve an optical precision of ~10 μm for the printing. The resulting skeleton presents an outer diameter of $D_o = 750$ μm and a length of $l = 3.0$ mm. Its design features a central lumen of diameter $d_o = 460$ μm, intended for arranging the fiber bundle. Additionally, there are four peripheral holes, each with a diameter of $d_h = 130$ μm, arranged on a concentric circle with a diameter $d = 600$ μm. Three of these peripheral holes are spaced 120° apart and designated for the light guide fibers. The fourth hole, serving as the functional channel, is positioned precisely at the midpoint between two of the light guide fibers, forming a central angle of 60° with them. Furthermore, to address the challenges posed by the low strength and printing difficulties associated with the ultrathin fillets connecting the peripheral holes to the central lumen, we have modified the design by resecting

these fillets into parallel planes spaced $h = 80$ μm apart. The detailed CAD model of the skeleton can be seen in Fig. S6a.

To assemble the probe, meticulous attention is required to ensure that each component is inserted correctly into its designated hole in the skeleton. Key elements include a fiber bundle with diameter of 450 μm (MBI-450S, SUNMO plastic optical fiber Inc., Shenzhen, China), three standard light guide fibers with 125 μm diameter (IR105/125-AC, Fibestar Technology Co., Ltd, Beijing, China), and one functional tool (micro tube with an outer/inner diameter of 100/50 μm, or laser fiber with 125 μm diameter). Then, the assembly is secured by dipping the UV glue and irradiating with UV light (395 nm) for 30 s. The top view of the assembled probe have been captured by digital microscope (Dino-Lite AM73915MZT(R10)), shown in Fig. S1b.

To generate the magnetic skin for the continuum robot, we employ the magnetic spray technique. As shown in Fig. S1c, we initially mix the silicone rubber precursor A and B (Ecoflex 00-30, Smooth-on Inc.) and iron micro-particles (5 μm diameter, Guangzhou Metallurgy Co., Ltd) in a beaker, maintaining a weight ratio of 1:1:1 (A:B:iron). After vigorously stirring the mixture for five min and degassing it for eight min, we obtain a homogeneous magnetic elastomer, referred to as M-spray. Here, we apply a rubber tube with an outer/inner diameter of 3.0/2.5 mm as the soft sheath body. Using a pressure spray kettle, we spray a thin layer of this magnetic elastomer onto the surface of the probe/sheath tip. After allowing the magnetic elastomer to cure for 8 h under room temperature, we obtain a magnetic probe/sheath tip. To ensure the integrity of the probe body composed of fiber array, we coat the slender body of the probe with a thin layer of pure elastomer, free of iron particles, using a similar spraying approach. The fabricated fiber-based probe and soft sheath with magnetic elastomer tip can be found in Fig. S1d.

To further minimize the friction between the channel wall and the probe/sheath, an additional thin layer of hydrogel skin is applied to the entire slender body[36]. According to Fig. S1e, the initial step involves coating the probe/sheath with an elastomer skin. Subsequently, the slender body is immersed in an organic solution (Isopropanol, Aladdin Chemistry, Shanghai, China) including hydrophobic initiator (Benzophenone, Aladdin Chemistry, Shanghai, China) for 3–5 min (Fig. S1e–ii). After immersion, it is dried using nitrogen flow. Next, the dried body is immersed in a hydrogel monomer solution (Acrylamide, Aladdin Chemistry, Shanghai, China) containing hydrophilic initiator (α-Ketoglutaric acid, Aladdin Chemistry, Shanghai, China) and cured under UV light (395 nm) for 30 min (Fig. S1e–iii). Following this, a thin layer of hydrogel skin is formed on the elastomer surface (Fig. S1e–iv). Finally, with a gentle rinse of deionized water for 24 h, the fully coated probe/sheath is ready for use (Fig. S1e–v). The generated hydrogel skin on the elastomer surface can be seen in Fig. S1f.

Development of the back-end advancing platform

To facilitate the robotic advancing of both the soft sheath and the integrated probe, we have devised a corresponding back-end advancing platform, depicted in Fig. S21. This platform comprises two parts, including the mechanical subsystem and the control subsystem.

For the mechanical part, a ball-screw motor module with 600 mm stroke (denoted as module 1) is securely mounted on the optical base. Additionally, another small ball-screw motor module with a stroke of 100 mm (denoted as module 2) is firmly attached to the slider of module 1. Then, a stepper motor together with a pair of gears (denoted as module 3) are assembled to the rear plate of the module 2. Two tubular supports are correspondingly affixed, one to the slider of module 2 and the other to the rear plate of module 1. Next, the proximal end of the sheath is securely fastened to the upper gear via the support on the module 1. Lastly, the probe is mounted onto the support on the slider after passing through the soft sheath and connecting to the optical system.

With this platform, the soft sheath is endowed with two motion DOF, including the advancing/retrieving motion enabled by module 1 and the rotating motion provided by module 3. Notably, the rotating DOF serves as an auxiliary to the advancing DOF, simulating a drilling-like motion, thereby enhancing interventional capabilities when encountering resistance. On the other hand, the probe is only facilitated with the advancing/retrieving DOF.

To activate the series of modules, we developed a control subsystem, primarily consisting of a PC monitor, an Arduino controller (Arduino Mega2560), three motor drivers, a WIFI receiver, a remote control, and a DC power supply. The PC monitor serves as a central hub, loading the program to the Arduino controller and simultaneously receiving feedback from both the controller and the optical system. The remote control, connected wirelessly through the WIFI receiver, allows the physician to execute commands, which are designated on the buttons. Finally, the motor drivers function as a bridge, converting the commands from the controller into actions for the motor modules.

Scanning imaging

To demonstrate the scanning imaging function, we employ a pattern of modified Bauhinia flower as our target. Prior to the experiment, the probe is manually aligned to capture the central star of the leaf and achieve an initial distance of ~60 μm between the probe's tip and the target. Subsequently, guided by the designed Archimedes spiral trajectory shown in Fig. 4f, the probe tip is actuated by the Helmholtz coil system to follow a similar path (Fig. S29) and captures the leaf information simultaneously. The stitching process of the image mosaics (5-s interval) of the leaf pattern is presented in Fig. S30. Initially, only the star symbol is recorded. Over time, after 80 s, the star and three surrounding "CITYU" words became roughly distinguishable. Eventually, a complete image of one leaf from the bauhinia flower pattern has been presented. To assess the stitching accuracy, we compare the real pattern with the stitched image and find a RMSE of less than 9 pixels (Fig. S31).

Ex vivo interventional experiments

To demonstrate the integrated functional operations within an ex vivo porcine model, we initially conducted interventional experiments to validate the navigation and accessing capability of the proposed continuum robot. With the approvement of the institutional animal care and use committee (IACUC) (Shenzhen Advanced Medical Services Co., Ltd), three porcine lung model are utilized for the trials, where real-time tracking of the robot's position during the trials is achieved using digital subtraction angiography (DSA, CGO-2100, Beijing Wandong Medical Equipment Co., Ltd). For actuation purposes, a permanent magnet ($50 \times 50 \times 25$ mm^3) and the back-end advancing platform are respectively employed to steer and advance the sheath/probe tip into the desired bronchus channel. As depicted in the schematic on the right side of Fig. 5a, various end bronchus of the bronchial tree channels would be accessed.

The interventional process inside the porcine lung sample I is illustrated in Fig. S39a. Initially, the soft sheath equipped with a magnetic tip is introduced into the right lung at 40.6 s and subsequently the down-left lung bronchus within ~110 s. Later, the inner magnetic probe is protruded to reach the end bronchus at 180 s. According to the anatomical results shown in Fig. S39b, the end bronchus that the probe tip accessed is with a diameter of ~1.0 mm.

To further demonstrate the adaptability of the proposed continuum robot, we showcase the similar interventional procedures within another porcine model (sample II). The DSA images that reports the process have been presented in Fig. S40a. The sheath is first steered by the magnetic field to access the bronchus located in the middle-right lung within ~140 s. Then, the probe is advanced to enter

the end bronchus at 160 s. The anatomical examination also verifies the successful accessing of the end bronchus (Fig. S40b).

Data collection and statistical analysis

Solidworks 2016 is employed to show the schematic illustration and the modeling of the fiberscopic robot and the corresponding imaging/advancing system. To capture the images and videos shown in this study, MindVision Camera Platform Setup (2.1.10.142), DinoCapture 2.0, and Xiaomi 8 UD are utilized. The software Arduino 1.8.5 is used for controlling of the rear-end advancing platform and collecting the position data of all the motors. All the data extracted from the images and videos are with the help of MATLAB R2021b. Origin 2021 and Microsoft Visio 2016 are correspondingly employed to plot the data and present the entire figures. ImageViewer X64 V2.0.4.0422 is employed to read and analyze H&E images.

Reporting summary

Further information on research design is available in the Nature Portfolio Reporting Summary linked to this article.

Data availability

All the data supporting the findings of this study are available within this article and its Supplementary Information. Any additional information can be obtained from corresponding authors upon request. Source data are provided with this paper.

References

1. Cianchetti, M., Laschi, C., Menciassi, A. & Dario, P. Biomedical applications of soft robotics. *Nat. Rev. Mater.* **3**, 143–153 (2018).
2. Runciman, M., Darzi, A. & Mylonas, G. P. Soft robotics in minimally invasive surgery. *Soft Robot.* **6**, 423–443 (2019).
3. Yang, G.-Z. et al. The grand challenges of Science Robotics. *Sci. Robot.* **3**, eaar7650 (2018).
4. Nazarian, S. et al. Feasibility of real-time magnetic resonance imaging for catheter guidance in electrophysiology studies. *Circulation* **118**, 223–229 (2008).
5. J. Ding et al. Design and coordination kinematics of an insertable robotic effectors platform for single-port access surgery. *IEEE ASME Trans Mechatron*, 1612-1624 (IEEE, 2013).
6. Flora, E. D., Wilson, T. G., Martin, I. J., O'Rourke, N. A. & Maddern, G. J. A review of natural orifice translumenal endoscopic surgery (NOTES) for intra-abdominal surgery: experimental models, techniques, and applicability to the clinical setting. *Ann. Surg.* **247**, 583–602 (2008).
7. Frolich, A. M. et al. Angiographic reconstructions from whole-brain perfusion CT for the detection of large vessel occlusion in acute stroke. *Stroke* **43**, 97–102 (2012).
8. Rucker, D. C. & Webster Iii, R. J. Statics and dynamics of continuum robots with general tendon routing and external loading. *IEEE Trans. Robot.* **27**, 1033–1044 (2011).
9. Zhang, T. et al. Millimeter-scale soft continuum robots for large-angle and high-precision manipulation by hybrid actuation. *Adv. Intell. Syst.* **3**, 2000189 (2021).
10. Shi, J. et al. Stiffness modelling and analysis of soft fluidic-driven robots using Lie theory. *Int. J. Robot. Res.* **43**, 354–384 (2023).
11. Miao, J. et al. Flagellar/ciliary intrinsic driven mechanism inspired all-in-one tubular robotic actuator. *Engineering* **23**, 170–180 (2023).
12. Kim, Y., Cheng, S. S. & Desai, J. P. Active stiffness tuning of a spring-based continuum robot for MRI-guided neurosurgery. *IEEE Trans. Robot* **34**, 18–28 (2018).
13. Kim, Y., German, A. P., Liu, S. & Zhao, X. Ferromagnetic soft continuum robots. *Sci. Robot.* **33**, eaax7329 (2019).
14. Edelmann, J., Petruska, A. J. & Nelson, B. J. Magnetic control of continuum devices. *Int. J. Robot. Res.* **36**, 68–85 (2017).
15. Tiryaki, M. E., Elmacıoğlu, Y. G. & Sitti, M. Magnetic guidewire steering at ultrahigh magnetic fields. *Sci. Adv.* **9**, eadg6438 (2023).
16. Florin, T. A., Plint, A. C. & Zorc, J. J. Viral bronchiolitis. *Lancet* **389**, 211–224 (2017).
17. Ribeiro, J. C. et al. Aquaporins and (in)fertility: more than just water transport. *Biochim. Biophys. Acta Mol. Basis Dis.* **1867**, 166039 (2021).
18. GOPESH, T. et al. Soft robotic steerable microcatheter for the endovascular treatment of cerebral disorders. *Sci. Robot.* **6**, eabf0601 (2021).
19. Ren, H. et al. An achromatic metafiber for focusing and imaging across the entire telecommunication range. *Nat. Commun.* **13**, 4183 (2022).
20. Orth, A., Ploschner, M., Wilson, E. R., Maksymov, I. S. & Gibson, B. C. Optical fiber bundles: ultra-slim light field imaging probes. *Sci. Adv.* **5**, eaav1555 (2019).
21. Wen, Z. et al. Single multimode fibre for in vivo light-field-encoded endoscopic imaging. *Nat. Photonics* **17**, 679–687 (2023).
22. Li, J. et al. Ultrathin monolithic 3D printed optical coherence tomography endoscopy for preclinical and clinical use. *Light Sci. Appl.* **9**, 124 (2020).
23. Gassino, R. et al. A fiber optic probe for tumor laser ablation with integrated temperature measurement capability. *J. Lightwave Technol.* **35**, 3447–3454 (2017).
24. Zhang, S., Zhang, E. Z., Beard, P. C., Desjardins, A. E. & Colchester, R. J. Dual-modality fibre optic probe for simultaneous ablation and ultrasound imaging. *Commun. Eng.* **1**, 20 (2022).
25. G. Pittiglio et al. Personalized magnetic tentacles for targeted photothermal cancer therapy in peripheral lungs. *Commun. Eng.* **2**, 50 (2023).
26. Yang, X. et al. An agglutinate magnetic spray transforms inanimate objects into millirobots for biomedical applications. *Sci. Robot.* **5**, abc8191 (2020).
27. Oka, K., Seki, T., Naganawa, A., Kim, K. & Chiba, T. A novel ultrasmall composite optical fiberscope. *Surg. Endosc.* **25**, 2368–2371 (2011).
28. Zou, Y., Chau, F. S. & Zhou, G. Ultra-compact optical zoom endoscope using solid tunable lenses. *Opt. Express* **25**, 20675–20688 (2017).
29. Zhuang, J., Wang, Z., Liao, X., Gao, B. & Cheng, L. Hierarchical spiral-scan trajectory for efficient scanning ion conductance microscopy. *Micron* **123**, 102683 (2019).
30. Capitanio, S., Nordin, A. J., Noraini, A. R. & Rossetti, C. PET/CT in nononcological lung diseases: current applications and future perspectives. *Eur. Respir. Rev.* **25**, 247–258 (2016).
31. Ilie, M. & Hofman, P. Pros: can tissue biopsy be replaced by liquid biopsy? *Transl. Lung Cancer Res.* **5**, 420–423 (2016).
32. Esther, C. R. Jr et al. Mucus accumulation in the lungs precedes structural changes and infection in children with cystic fibrosis. *Sci. Transl. Med.* **11**, eaav3488 (2019).
33. Manzari, M. T. et al. Targeted drug delivery strategies for precision medicines. *Nat. Rev. Mater.* **6**, 351–370 (2021).
34. Singh, A. P., Biswas, A., Shukla, A. & Maiti, P. Targeted therapy in chronic diseases using nanomaterial-based drug delivery vehicles. *Signal Transduct. Target Ther.* **4**, 33 (2019).
35. Hsiao, C. Y., Yang, S. C., Alalaiwe, A. & Fang, J. Y. Laser ablation and topical drug delivery: a review of recent advances. *Expert Opin. Drug Deliv.* **16**, 937–952 (2019).
36. Yu, Y. et al. Multifunctional "Hydrogel Skins" on diverse polymers with arbitrary shapes. *Adv. Mater.* **31**, e1807101 (2019).

Acknowledgements

This work was funded by National Natural Science Foundation of China (NSFC)/Research Grants Council (RGC) Joint Research Scheme (Grant No. N_HKUST638/23, Y.S., Grant No. 62361166630, W.S.), National Natural Science Foundation of China (Grant No. 62273323, W.S.), Shenzhen-Hong Kong-Macau Science and Technology Project (Grant

No. SGDX20201103093003017, Y.S.), Hong Kong RGC General Research Fund (Grant No. 16203923, Y.S.), and Guangdong Basic and App1ied Basic Research Foundation (Grant No. GDST24EG02, Y.S.).

Author contributions

Conceptualization, Y.S.; methodology, T.Z., and G.L.; software, G.L., and H.R.; validation, T.Z., G.L., H.R., L.Y., X.Y., R.T., and Y.T.; formal analysis, T.Z., and G.L.; data curation, T.Z., G.L., H.R., and H.Z.; visualization, D.G., H.Z.; writing—original draft preparation, T.Z.; writing—review and editing, T.Z. and Y.S.; supervision, Y.S.; project administration, W.S. and Y.S.; funding acquisition, W.S. and Y.S. All authors have read and agreed to the published version of the manuscript.

Competing interests

The authors declare no competing interests.

Additional information

Supplementary information The online version contains supplementary material available at https://doi.org/10.1038/s41467-024-55199-6.

Correspondence and requests for materials should be addressed to Yajing Shen.

Peer review information *Nature Communications* thanks the anonymous reviewers for their contribution to the peer review of this work. A peer review file is available.